metals

MDPI

Article

Effects of Alloying Elements Addition on Delayed Fracture Properties of Ultra High-Strength TRIP-Aided Martensitic Steels

Tomohiko Hojo [1,*], Junya Kobayashi [2], Koh-ichi Sugimoto [3], Akihiko Nagasaka [4] and Eiji Akiyama [1]

1 Institute for Materials Research, Tohoku University, Sendai 980-8577, Japan; akiyama@imr.tohoku.ac.jp
2 Department of Mechanical Systems Engineering, College of Engineering, Ibaraki University, Ibaraki 316-8511, Japan; junya.kobayashi.jkoba@vc.ibaraki.ac.jp
3 Department of Mechanical Systems Engineering, School of Science and Technology, Shinshu University, Nagano 380-8553, Japan; sugimot@shinshu-u.ac.jp
4 Department of Mechanical Engineering, National Institute of Technology, Nagano College, Nagano 381-8550, Japan; nagasaka@nagano-nct.ac.jp
* Correspondence: hojo@imr.tohoku.ac.jp; Tel.: +81-22-215-2062

Received: 20 November 2019; Accepted: 17 December 2019; Published: 19 December 2019

Abstract: To develop ultra high-strength cold stamping steels for automobile frame parts, the effects of alloying elements on hydrogen embrittlement properties of ultra high-strength low alloy transformation induced plasticity (TRIP)-aided steels with a martensite matrix (TM steels) were investigated using the four-point bending test and conventional strain rate tensile test (CSRT). Hydrogen embrittlement properties of the TM steels were improved by the alloying addition. Particularly, 1.0 mass% chromium added TM steel indicated excellent hydrogen embrittlement resistance. This effect was attributed to (1) the decrease in the diffusible hydrogen concentration at the uniform and fine prior austenite grain and packet, block, and lath boundaries; (2) the suppression of hydrogen trapping at martensite matrix/cementite interfaces owing to the suppression of precipitation of cementite at the coarse martensite lath matrix; and (3) the suppression of the hydrogen diffusion to the crack initiation sites owing to the high stability of retained austenite because of the existence of retained austenite in a large amount of the martensite–austenite constituent (M–A) phase in the TM steels containing 1.0 mass% chromium.

Keywords: TRIP-aided steels; microalloying; hydrogen embrittlement; retained austenite

1. Introduction

Recently, ultra high-strength steels with a tensile strength of more than 980 MPa have been applied for automobile frame parts to improve the impact safety and fuel efficiency of the vehicles. In the ultra high-strength steels, 980–1180 MPa grade transformation induced plasticity (TRIP)-aided bainitic ferrite steels (TBF steels) associated with transformation induced plasticity (TRIP) [1] of retained austenite have been used for the ultra high-strength automobile structural parts because of the excellent press formability [2], impact properties [3], fatigue properties [4] and hydrogen embrittlement (delayed fracture) resistance [5]. In addition, 1500 MPa grade hot stamping ultra high-strength steels [6] have been applied for the part of automobile impact safety components such as center pillars and side impact bars. Generally, it is known that hydrogen embrittlement remarkably appears in the structural high strength bolts when the tensile strength of steels increases to more than 980 MPa. Thus, occurrence of the hydrogen embrittlement becomes a serious problem in the automobile ultra high-strength steel sheets.

Among the 1470 MPa grade ultra high-strength steels, the ultra high-strength TRIP-aided martensitic steels (TM steels) are expected to be applied for automobile structural parts, as the TM steels exhibit ultra high-strength of 1500 MPa grade owing to the martensite lath matrix and excellent formability because of TRIP effects of retained austenite existing in the martensite–austenite constituent (M–A) phase. However, further strengthening of the TM steels requires improvement of hardenability and tailoring the uniform microstructure. In this study, we produced the TM steels microalloyed with elements such as chromium, molybdenum, nickel, titanium, and boron and investigated the hydrogen embrittlement properties of steels using a constant load test and a conventional strain rate tensile test (CSRT) [7–9], aiming at applying the steels to the automotive structural parts.

2. Materials and Methods

In this study, six kinds of cold rolled 0.2C–1.5Si–1.5Mn (mass%) steel sheets with a thickness of 1.2 mm with microalloying elements of niobium, chromium, molybdenum, nickel, boron, and titanium were prepared. The chemical compositions of these steels are listed in Table 1. The martensite transformation start temperature (M_S) [10] calculated by the following equation is also listed in the Table.

$$M_S\ (^\circ\mathrm{C}) = 550 - 361 \times (\%\mathrm{C}) - 39 \times (\%\mathrm{Mn}) - 0 \times (\%\mathrm{Si}) + 30 \times (\%\mathrm{Al}) - 5 \times (\%\mathrm{Mo}), \quad (1)$$

where %C, %Mn, %Si, %Al, and %Mo in mass% are alloying contents in the steels, respectively. Moreover, hardenability of steels defined as a product of the multiplying factors (ΠIfi) [11], estimated by the following equation, is also shown in Table 1.

$$\begin{aligned}\Pi\mathrm{Ifi} = {} & (1 + 0.64\%\mathrm{Si}) \times (1 + 4.10\%\mathrm{Mn}) \times (1 + 2.83\%\mathrm{P}) \times (1 - 0.62\%\mathrm{S}) \times (1 + 2.33\%\mathrm{Cr}) \times \\ & (1 + 0.52\%\mathrm{Ni}) \times (1 + 3.14\%\mathrm{Mo}) \times (1 - 0.27\%\mathrm{Cu}) \times (1 + 1.5(0.9 - \%\mathrm{C})),\end{aligned} \quad (2)$$

where (1 + 1.5 (0.9 − %C)) was added when B was added.

The TRIP-aided steels with martensitic matrix were produced by annealing at 920 °C × 1200 s followed by partitioning treatment (T_p) at 250 °C for steels A and B and 350 °C for steels C, D, E, and F for 1000 s, as shown in Figure 1.

Retained austenite characteristics were analyzed by X-ray diffractometry (Rigaku Co. Ltd., RINT2000, Tokyo, Japan). Volume fraction of retained austenite (f_γ (vol.%)) was calculated from integrated intensity of 200_α, 211_α, 200_γ, 220_γ, and 311_γ diffraction peaks measured using CuKα radiation [12]. On the other hand, carbon concentration of retained austenite (C_γ (mass%)) was estimated by the following equation (3) [13] using an average lattice parameter (a_γ ($\times 10^{-10}$ m)) evaluated from 200_γ, 220_γ, and 311_γ peaks analyzed using CuKα radiation.

$$\begin{aligned}a_\gamma = {} & 3.5780 + 0.0330\mathrm{C}_\gamma + 0.00095\mathrm{Mn}_\gamma - 0.0002\mathrm{Ni}_\gamma + 0.0006\mathrm{Cr}_\gamma + 0.0056\mathrm{Al}_\gamma + 0.0220\mathrm{N}_\gamma + \\ & 0.0004\mathrm{Co}_\gamma + 0.0015\mathrm{Cu}_\gamma + 0.0051\mathrm{Nb}_\gamma + 0.0031\mathrm{Mo}_\gamma + 0.0039\mathrm{Ti}_\gamma + 0.0018\mathrm{V}_\gamma + 0.0018\mathrm{W}_\gamma,\end{aligned} \quad (3)$$

where Mn_γ, Ni_γ, Cr_γ, Al_γ, N_γ, Co_γ, Cu_γ, Nb_γ, Mo_γ, Ti_γ, V_γ, and W_γ represent alloying contents in austenite. In this study, the average content of each element in the steels was used.

The four-point bending cathode charging technique [5,8,14] was adopted to evaluate the hydrogen embrittlement properties of the steels using rectangular specimens of 65 mm in length, 10 mm in width, and 1.2 mm in thickness, with hydrogen charging in a 0.5 mol H_2SO_4 (FUJIFILM Wako Pure Chemical Co. Ltd., Sulfuric Acid, Japan) + 0.01 mol NH_4SCN (FUJIFILM Wako Pure Chemical Co. Ltd., Ammonium Thiocyanate, Japan) solution at 25 °C at a current density of 100 A/m^2. Hydrogen embrittlement properties were evaluated by delayed fracture strength (*DFS*), which is the maximum bending stress that does not cause failure of the specimen for 5 h.

Tensile tests of the steels were also carried out using a tensile testing machine (Shimadzu Co. Ltd., AG-X plus 100kN, Kyoto, Japan) at a crosshead speed of 1 mm/min at 25 °C without and with hydrogen charging. Tensile testing specimens were used with 15 mm in gauge length, 6 mm in

width, and 1.2 mm in thickness. Hydrogen embrittlement properties were evaluated by hydrogen embrittlement susceptibility (*HES*) calculated by the following equation.

$$HES = (1 - \varepsilon_1/\varepsilon_0) \times 100\%, \quad (4)$$

where ε_0 and ε_1 represent total elongation without and with hydrogen charging, respectively. Hydrogen charging to the tensile specimens was conducted by cathodic charging. A hydrogen charging solution of a 3% NaCl (FUJIFILM Wako Pure Chemical Co. Ltd., Sodium Chloride, Japan) + 3 g/L NH_4SCN was used, and the hydrogen charging condition was at a current density of 10 A/m^2, at 25 °C for 48 h.

Diffusible hydrogen concentration of the tensile specimens was measured by means of thermal desorption analysis (TDA) using a gas chromatography as a hydrogen detector (J-SCIENCE LAB Co. Ltd., GC-MS, Kyoto, Japan). Specimens were heated from room temperature to 800 °C at a heating rate of 200 °C/h. Diffusible hydrogen concentration (wt. ppm) was defined as a weight ppm of evolved hydrogen from room temperature to 150 °C corresponding to a first peak of the hydrogen evolution curve to specimen weight. The hydrogen charged specimens were kept in liquid nitrogen to prevent the hydrogen evolution from the specimen until hydrogen analysis.

Electron Back Scatter Diffraction Patterns (EBSD) analysis for the body centered cubic (bcc) phase was carried out in an area of 40 μm × 40 μm with step size of 0.2 μm. Inverse pole figure (IPF) and kernel average misorientation (KAM) maps were used to define the initial microstructures and the strain distributions after the tensile test in this study. Moreover, image quality (IQ) value was used to estimate an area fraction of the M–A phase. The area fraction of the M–A phase was defined as a total fraction of IQ value below 50.

In this study, the four-point bending constant load test and conventional strain rate tensile test were conducted at different hydrogen charging conditions. Four-point bending tests were conducted at relatively low stress with a high hydrogen concentration, whereas stress and plastic strain were continuously increased during conventional strain rate tensile tests with a low hydrogen concentration. These two testing and hydrogen charging methods were adopted to evaluate the hydrogen embrittlement properties of the microalloyed TM steels at a wide range of conditions of stress, plastic strain, and hydrogen concentration.

Table 1. Chemical compositions (mass%), martensite transformation start temperature (M_S) and hardenability (ΠIfi) of transformation induced plasticity (TRIP)-aided steels with a martensite matrix (TM steels).

Steel	C	Si	Mn	Ni	Cr	Mo	Al	Nb	Ti	B	M_S	ΠIfi
A	0.20	1.50	1.50	-	-	-	0.039	-	-	-	420	14.60
B	0.20	1.52	1.50	-	-	-	0.039	0.05	0.02	0.0018	420	29.21
C	0.21	1.49	1.50	-	0.50	-	0.04	0.05	-	-	407	30.55
D	0.20	1.49	1.50	-	1.00	-	0.04	0.05	-	-	401	46.99
E	0.18	1.48	1.49	-	1.02	0.20	0.043	0.05	-	-	407	76.82
F	0.21	1.49	1.49	1.52	1.00	0.20	0.034	0.049	-	-	370	135.8

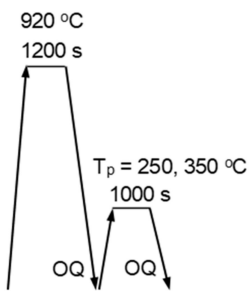

Figure 1. Heat treatment diagram of transformation induced plasticity (TRIP)-aided steels with a martensite matrix (TM steels). OQ represents oil quenching.

3. Results

3.1. Microstructure and Tensile Properties

Figure 2 shows inverse pole figure (IPF) maps of the TM steels analyzed by EBSD. Typical transmission electron micrographs of the TM steels are shown in Figure 3. The martensite lath matrix of the TM steels became fine and uniform owing to the addition of alloying elements in comparison with that of steel A (Figures 2 and 3). The TM steels consisted of wide lath martensite, a hard and narrow M–A phase, and retained austenite (Figure 3). Retained austenite film existed at lath boundaries and the M–A phase consisted of narrow martensite and retained austenite in steel A. In contrast, retained austenite film was not observed at martensite lath boundaries in steels B–F, although fine retained austenite existed in the M–A phase. Precipitation of cementite was suppressed by the alloying addition in the TM steels, although it was confirmed that cementite precipitated at coarse lath martensite in steel A without alloying addition (Figure 3).

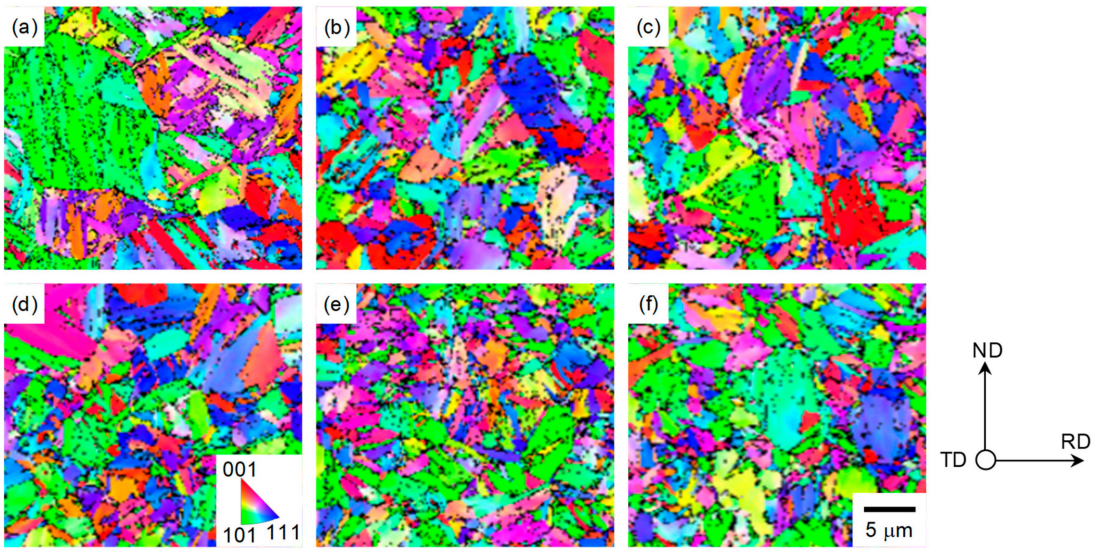

Figure 2. Microstructures of TM steels of steels (**a**) A, (**b**) B, (**c**) C, (**d**) D, (**e**) E, and (**f**) F partitioned at 250 or 350 °C. RD, ND and TD represent rolling, normal, and transverse directions, respectively.

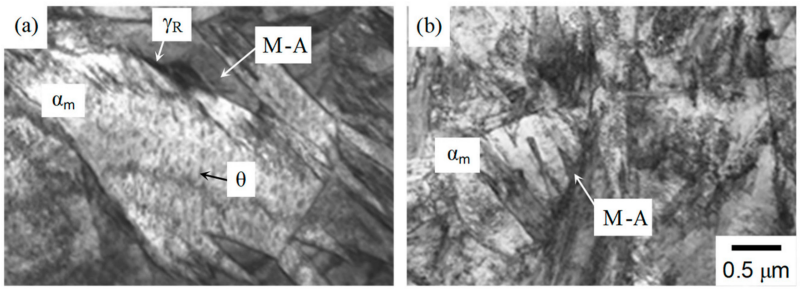

Figure 3. Transmission electron micrographs of TM steels of steels (**a**) A and (**b**) D partitioned at (**a**) 250 and (**b**) 350 °C, in which γ_R, α_m, θ, and M–A represent retained austenite, martensite, cementite, and martensite–austenite constituent (M–A) phase, respectively.

Table 2 shows the retained austenite characteristics, area fraction of the M–A phase, tensile properties, and prior austenite grain size of the TM steels. The initial volume fractions of retained austenite ($f_{\gamma 0}$s) were between 1.8 vol.% and 2.2 vol.%, and its carbon concentrations ($C_{\gamma 0}$s) were 0.52 mass%–1.32 mass%. $f_{\gamma 0}$s were slightly changed by the alloying addition. On the other hand, chromium addition increased $C_{\gamma 0}$ and complex addition of titanium–boron, chromium–molybdenum, and nickel–chromium–molybdenum significantly decreased $C_{\gamma 0}$ in the TM steels compared with steel

A. The area fraction of M–A phases ($f_{\text{M–A}}$s) of the TM steels was 20.0% or more. Alloying addition increased $f_{\text{M–A}}$ in the TM steels.

Table 2. Tensile properties, retained austenite characteristics, area fraction of the martensite–austenite constituent (M–A) phase, and prior austenite grain size of TM steels.

Steel	*TS*	*YS*	*TEl*	*UEl*	$f_{\gamma 0}$	$C_{\gamma 0}$	$f_{\text{M–A}}$	*d*
A	1422	1137	12.6	4.2	2.1	1.20	20.0	22.6
B	1490	1292	13.9	5.6	2.0	1.32	21.4	16.0
C	1445	1331	12.6	4.7	1.8	0.75	22.3	14.3
D	1498	1386	14.2	5.1	2.2	1.19	20.7	14.8
E	1496	1376	15.3	5.1	2.2	0.52	24.9	11.3
F	1547	1396	14.1	4.3	1.9	0.96	26.7	12.7

TS (MPa): tensile strength, *YS* (MPa): yield strength, *TEl* (%): total elongation, *UEl* (%): uniform elongation, $f_{\gamma 0}$ (vol.%): initial volume fraction of retained austenite, $C_{\gamma 0}$ (mass%): initial carbon concentration of retained austenite, $f_{\text{M–A}}$ (%): area fraction of M–A phase, *d* (μm): prior austenite grain diameter.

Tensile strengths (*TS*s) of the TM steels were between 1422 and 1542 MPa, and total elongations (*TEl*s) exhibited 12.6–15.3%. Alloying addition to the TM steels resulted in both high strength and large elongation compared with steel A, and they exhibited an excellent strength–ductility balance. Particularly, the tensile strength (*TS*) increased owing to the Ni–Cr–Mo complex addition, and the total elongation (*TEl*) was increased by the complex addition of Cr–Mo.

The prior austenite grain size (*d*) of steel A was 22.6 μm, and alloyed TM steel exhibited an obviously decreased prior austenite grain size in the range of 11.3–16.0 μm.

3.2. Hydrogen Enbrittlement Properties Evaluated by Four-Point Bending Test

Typical applied stress-fracture time plots of the TM steels are shown in Figures 4 and 5 shows relationship between delayed fracture strength (*DFS*), which is the maximum bending stress causing no failure of specimen for 5 h and tensile strength (*TS*). In the all steels, time to fracture (t_f) was shortened with applied stress (σ_A). Steel C alloyed with 0.5 mass% chromium possessed a long time to failure and increased *DFS* in comparison with other TM steels. Although steel D alloyed with 1.0 mass% chromium fractured earlier at a high applied bending stress region than steel A, *DFS* of steel D was higher than that of steel A. On the other hand, steel E co-alloyed with chromium and molybdenum fractured in short time compared with the steel A, and *DFS* was similar to that of steel A. From Figure 5, *DFS* of about 750–850 MPa was achieved in steel B alloyed with titanium and boron and C with 0.5 mass% chromium. All of the steels with alloying addition except for steel E showed higher *DFS* than steel A, though the *TS* of the alloyed steels was higher than that of steel A. Steel E showed slightly low *DFS* compared with steel A, but its *TS* was higher than that of steel A. The relationship between *DFS* and *TS* of the alloyed steels in the band is shown by the hatch in the figure, and the relative position of the band to the data point of steel A indicated that the alloying additions had a positive effect on improving the resistance of the TM steel against hydrogen embrittlement.

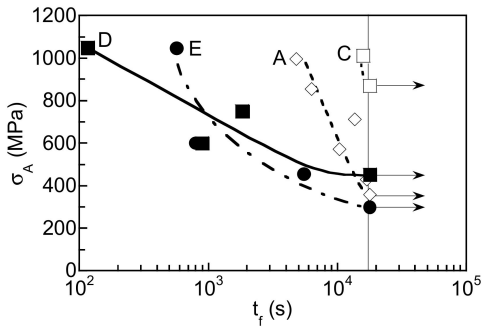

Figure 4. Typical delayed fracture curves of TM steels of steels A, C, D, and E.

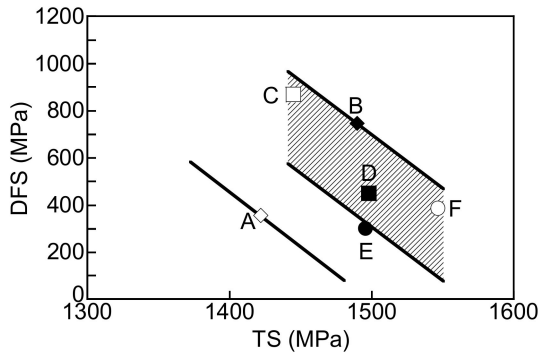

Figure 5. Variations in delayed fracture strength (*DFS*) as a function of tensile strength (*TS*) in TM steels.

Figure 6 shows the fracture surface of the TM steels after four-point bending testing. In Figure 6, four-point bending tests were carried out at an applied bending stress of 70–80 MPa higher than the value of *DFS*. Fracture surfaces of the steels indicated a mixed fracture of intergranular and transgranular fractures. The ratio of intergranular fracture surface was high for steels A and E, suggesting the correspondence of the morphologies with the susceptibilities evaluated by *DFS*. It was noted that a small unit crack path was observed in the alloyed TM steels compared with steel A, presumably owing to the small size of prior austenite grain, as shown in Table 2. The morphology of the fracture surface of steel B was similar to that of other microalloyed TM steels.

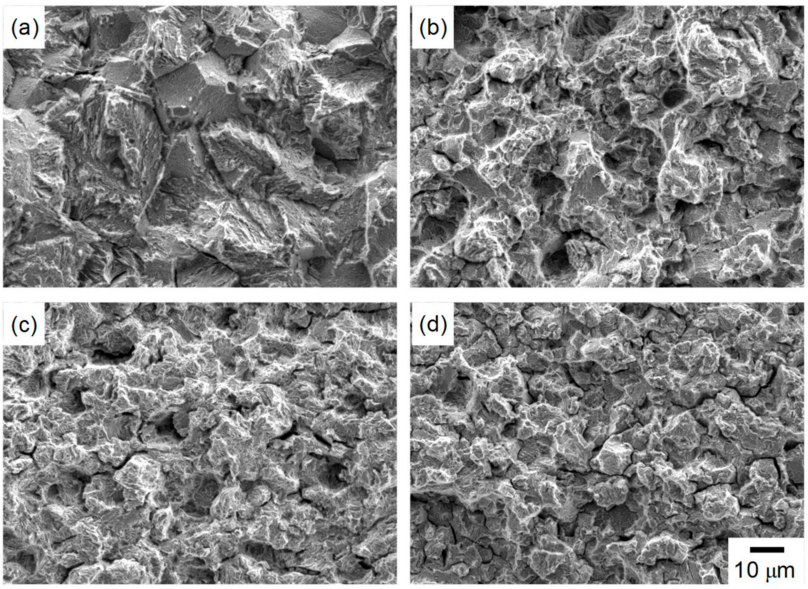

Figure 6. Typical fracture surfaces of steels (**a**) A, (**b**) C, (**c**) D, and (**d**) E after four-point bending testing.

3.3. Hydrogen Embrittlement Properties Evaluated by Tensile Test

Figure 7 shows typical stress–strain curves without and with hydrogen charging in the TM steels. Steels A and E charged with hydrogen fractured in an early stage with a deterioration of local elongation, although the stress–strain behavior up to a maximum stress with hydrogen was almost the same as that without hydrogen. A decrease in the local elongation hardly appeared in steels C and D with additive chromium of 0.5 mass% and 1.0 mass%, respectively. The relationships between hydrogen embrittlement susceptibility (*HES*) and yield strength (*YS*) and tensile strength (*TS*) are shown in Figure 8. Here, the low *HES* stands for excellent hydrogen embrittlement resistance; that is, *HES* = 0% means that hydrogen embrittlement never occurs. The hydrogen embrittlement susceptibility decreased owing to the addition of alloying elements in the TM steels, although yield and tensile strengths increased. Particularly, steel D alloyed with 1.0 mass% chromium exhibited low *HES*. Figure 9

shows fracture surfaces of steels A, C, D, and E without and with hydrogen charging. In all of the TM steels, dimple fracture occurred when tensile tests were conducted without hydrogen charging. The size of the dimple was quite small in steels A, C, and D, and fine and coarse dimple coexisted in steel E. On the other hand, steel A with hydrogen charging indicated a large size of dimple, whereas the fracture surface of the dimple decreased and that of quasi cleavage increased by the hydrogen charging in steel C. Moreover, steel D with hydrogen charging showed fine dimples, and steel E with hydrogen exhibited coarse dimple fracture, as well as the fracture surfaces of these steels without hydrogen charging. Hydrogen evolution curves of the TM steels charged with hydrogen are shown in Figure 10. It was confirmed that a large amount of hydrogen was evolved from room temperature to around 100 °C in the TM steels. The concentrations of diffusible hydrogen that was evolved at temperature between room temperature and 150 °C in the hydrogen evolution curves are listed in Table 3. The diffusible hydrogen concentration was increased by the addition of alloying element.

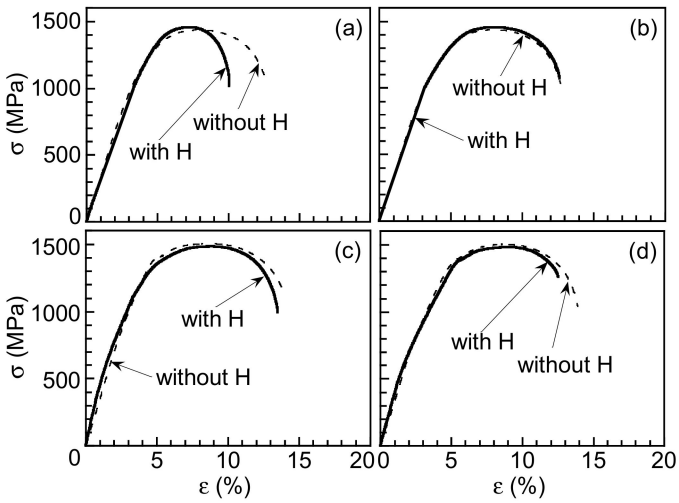

Figure 7. Typical stress–strain curves of steels (**a**) A, (**b**) C, (**c**) D, and (**d**) E without and with diffusible hydrogen.

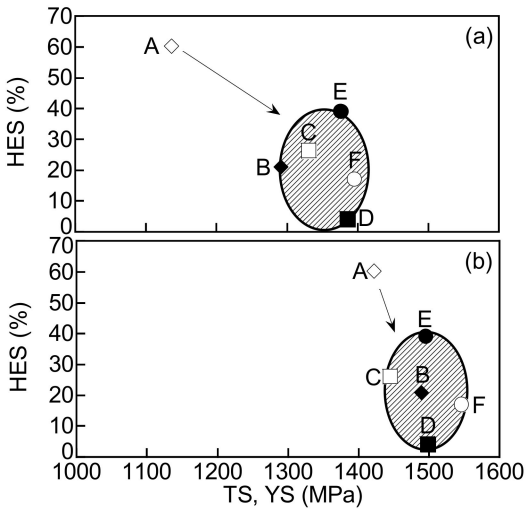

Figure 8. Relationships between hydrogen embrittlement susceptibility (*HES*) and (**a**) yield strength (*YS*) and (**b**) tensile strength (*TS*) in TM steels.

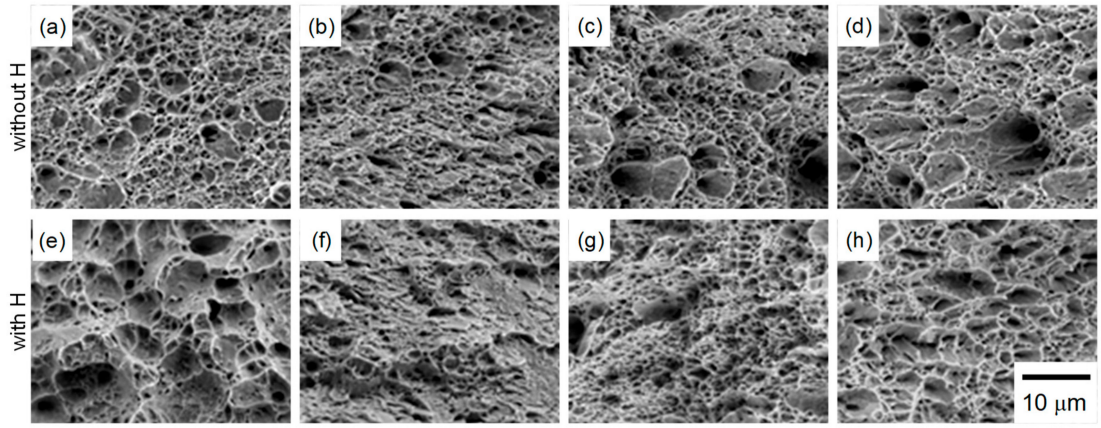

Figure 9. Scanning electron micrographs of the fracture surface tested by tensile testing of steels (**a**,**e**) A, (**b**,**f**) C, (**c**,**g**) D, and (**d**,**h**) E (**a**–**d**) without and (**e**–**h**) with hydrogen.

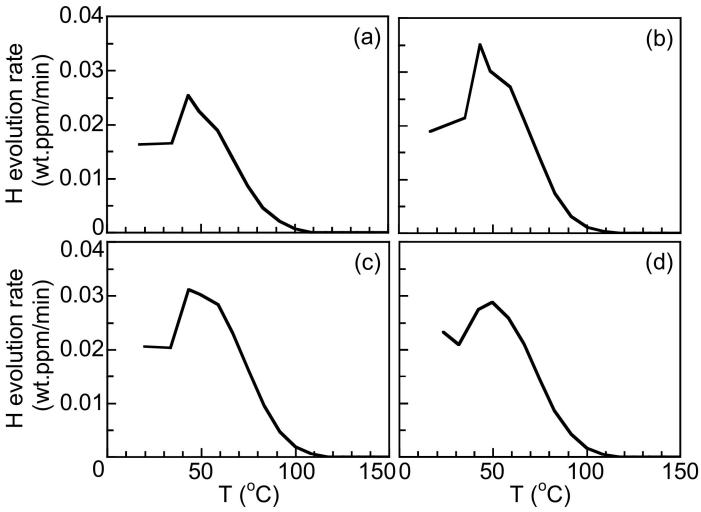

Figure 10. Hydrogen evolution curves of steels (**a**) A, (**b**) C, (**c**) D, and (**d**) E.

Table 3. Diffusible hydrogen concentration (H_D) of TM steels.

Steels	H_D (wt. ppm)
A	0.65
B	0.85
C	0.90
D	0.93
E	0.88
F	0.96

4. Discussion

Generally, the hydrogen embrittlement properties of the high-strength low alloy TRIP-aided steels, such as TBF steels containing a large amount of retained austenite, were affected by microstructural sizes, retained austenite characteristics, residual stress, and plastic strain distributions owing to the press forming and hydrogen concentration. Thus, we are going to discuss the relationship between hydrogen embrittlement properties and those dominant factors in the following parts.

4.1. Improvement of Hydrogen Embrittlement Properties by Refinement of Microstructure

It is known that the hydrogen embrittlement resistance of high strength steels depends on the size of a microstructure, namely, refinement of grain, packet, block, and lath sizes reduces the risk

of void and crack initiation, and improves the hydrogen embrittlement resistance because of the decrease in the facet size [15]. Moreover, it was suggested that hydrogen trapped at matrix/cementite interfaces decreased the hydrogen embrittlement resistance owing to the diffusion of hydrogen to the crack initiation sites such as the prior austenite grain and lath boundaries, as these interfaces are weak hydrogen trapping sites [16]. On the other hand, many investigations of the improvement of the hydrogen embrittlement resistance of high-strength steels have been strongly conducted with microalloying such as vanadium [17] and titanium [17,18], because matrix/metallic carbide coherency strain fields were the effective hydrogen trapping sites for the hydrogen embrittlement resistance due to the high hydrogen trapping energy.

The TM steels (steels B–E) in this study exhibited a small size of prior austenite grain, packet, block, and martensite lath because of the alloying addition (Figure 2). In addition, precipitation of cementite in the martensite laths and at the prior austenite grain boundaries was suppressed in the TM steel with 1.0 mass% chromium (steel D) (Figure 3). The refinement of prior austenite grain size owing to the addition of alloying element might be attributed to the precipitation of fine NbC during the hot rolling process, which suppressed growth of prior austenite grain [19]. Moreover, the improved hardenability of the microalloyed TM steels suppressed the precipitation of cementite in the martensite laths. It is also considered that the decrease in the M_S temperature delays the martensite transformation at quenching, and increases the amount of the M–A phase. The mechanism of such a microstructural change of the TM steels owing to the addition of alloying elements has been reported in previous reports [12,20,21].

It was considered that the microstructural change as mentioned above in the TM steels containing alloying elements improved hydrogen embrittlement resistance, namely, the hydrogen embrittlement resistance of the TM steels was improved by the suppression of the void and the crack initiation and propagation at the prior austenite grain, packet, block, and lath boundaries owing to the refinement of these hydrogen trapping sites, by the suppression of hydrogen trapping at martensite/cementite interfaces because of the no precipitation of cementite and because of the increase in the amount of the M–A phase. The effects of the M–A phase on the hydrogen embrittlement resistance are discussed later.

4.2. Effects of Stability of Retained Austenite on Hydrogen Embrittlement Properties

The hydrogen embrittlement properties were greatly affected by the retained austenite characteristics. In this study, the initial carbon concentration affected the hydrogen embrittlement resistance, although the initial volume fraction of retained austenite hardly affected *DFS* and *HES*, as shown in Figure 11. It was considered that transformation of unstable retained austenite to martensite was accelerated when unstable retained austenite absorbed hydrogen [5]. Moreover, the crack and void initiation was promoted by the desorption of hydrogen from transformed martensite because hydrogen solubility is significantly decreased when retained austenite (face centered cubic (fcc) phase) transforms to martensite (bcc phase) [22]. Hojo et al. [5] have investigated the hydrogen embrittlement resistance of aluminum and manganese added TRIP-aided bainitic ferrite (TBF) steels, and have reported that aluminum addition improved the hydrogen embrittlement resistance, whereas manganese addition worsened it. This was attributed to the increase in the stability of retained austenite in the aluminum added TBF steels, whereas the manganese addition to the TBF steels deteriorated the stability of retained austenite. The initial carbon concentration of steel D with additive chromium was similar to that in steel A, although the initial carbon concentration of steels B, E, and F was low compared with that of steel A. Thus, it was suggested that the chromium added TM steels exhibited excellent hydrogen embrittlement resistance owing to the suppression of martensite transformation during hydrogen embrittlement tests because of the high stability of retained austenite.

It was confirmed that the M–A phase formed at triple junctions of prior austenite grain in the TM steels, and retained austenite existed along the martensite lath boundaries in steel A (Figure 3a). However, in the TM steels alloyed with additive elements, retained austenite tended not to exist alone, but to coexist in the M–A phase. In addition, it was confirmed that the area fraction of the

M–A phase measured by image quality of EBSD increased owing to the alloying addition, as shown in Table 2. The filmy retained austenite in steel A might easily transform to martensite, assisted by straining or hydrogen despite the high initial carbon concentration of retained austenite, because retained austenite existed along relatively large and soft lath martensite, which formed during rapid cooling between austenitizing and ambient temperatures. On the other hand, it was considered that the stability of retained austenite in the TM steels alloyed with additive elements was high because fine retained austenite in the M–A phase was surrounded by the fine and hard martensite and, consequently, the martensite transformation of retained austenite in the M–A phase was suppressed [12,20,23]. Therefore, the TM steels with alloying addition exhibited excellent hydrogen embrittlement resistance.

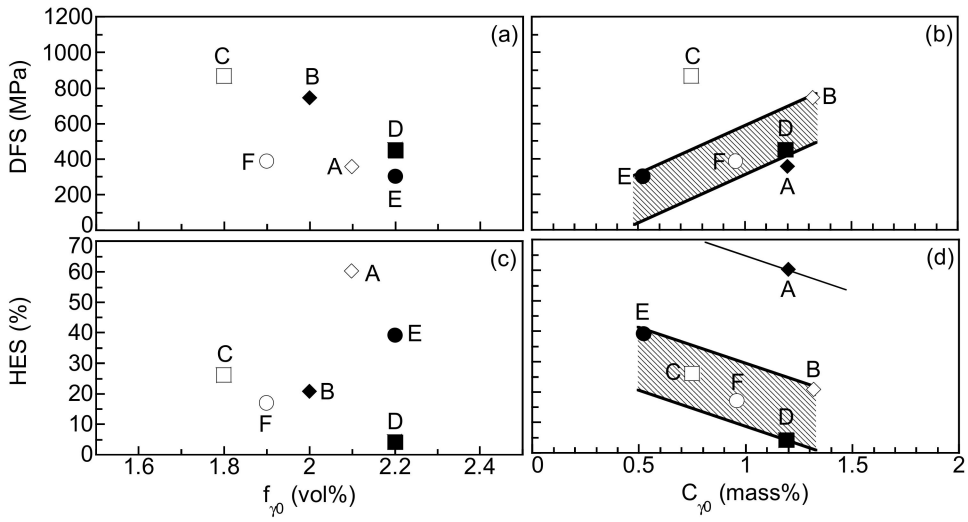

Figure 11. Variations in (**a**,**b**) delayed fracture strength (*DFS*) and (**c**,**d**) hydrogen embrittlement susceptibility (*HES*) as functions of (**a**,**c**) initial volume fraction of retained austenite ($f_{\gamma 0}$) and (**b**,**d**) its carbon concentration ($C_{\gamma 0}$) in TM steels.

4.3. Hydrogen Absorption Properties and Hydrogen Embrittlement Resistance

It is known that the amount of diffusible hydrogen and its trapping site in steels significantly affect the hydrogen embrittlement resistance of steels [24,25]. As shown in Figure 10 and Table 3, it was confirmed that a large amount of hydrogen was evolved from room temperature to around 100 °C in the TM steels. Furthermore, the addition of alloying element increased the amount of absorbed hydrogen. It is known that the hydrogen evolution from this temperature range is associated with hydrogen trapped at prior austenite grain and lath boundaries [26], at dislocations [25], at matrix/carbide interfaces [16], and in retained austenite [27,28] or at matrix/retained austenite interfaces [28]. In the TM steels, it was assumed that the amount of diffusible hydrogen in the TM steels increased because of a large amount of hydrogen trapped at refined prior austenite grain and lath boundaries owing to the addition of alloying element. However, the delayed fracture strength obtained by the four-point bending test was improved and hydrogen embrittlement susceptibility evaluated by the tensile test decreased, although diffusible hydrogen concentration increased compared with steel A, as shown in Figure 12. Presumably, areas of prior austenite grain and lath boundaries increased because prior austenite grain became small, and the width and length of laths decreased. Therefore, it was suggested that the occurrence of hydrogen embrittlement caused by void and crack nucleation, as well as their growth and propagation, were suppressed, resulting from low hydrogen concentration at prior austenite grain and lath boundaries, although the total amount of hydrogen trapped at prior austenite grain and lath boundaries was high owing to the increased area of boundaries.

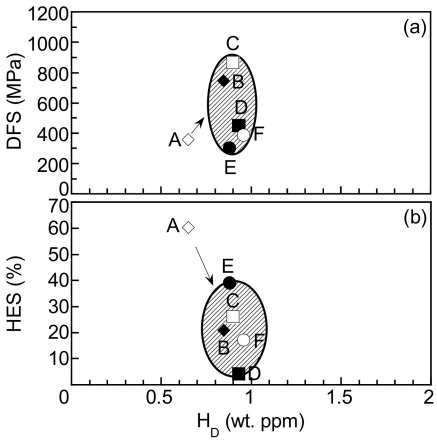

Figure 12. Relationships between (**a**) delayed fracture strength (*DFS*) and (**b**) hydrogen embrittlement susceptibility (*HES*) and diffusible hydrogen concentration (H_D) in TM steels.

4.4. Mechanism of Hydrogen Embrittlement in TM steels

Hydrogen embrittlement occurred with a large amount of plastic deformation given by the tensile test in this study. Accordingly, strain distributions at uniformly deformed part of tensile specimens in steels A and D were compared using kernel average misorientation (KAM) map analyzed by EBSD. The KAM maps and KAM value variations are shown in Figures 13 and 14, respectively. When tensile tests were carried out at the conventional strain rate without hydrogen charging, the KAM values of both steels A and D at both vicinity and inside of the packet and the lath boundaries slightly increased in comparison with those of as-heat treated steels (Figure 13). In addition, the high KAM value uniformly distributed in steel D compared with steel A (Figures 13 and 14). On the other hand, when tensile tests were conducted with hydrogen charging, the KAM value at vicinity of the packet and the lath boundaries of steel A significantly increased, and the distribution of the KAM value of steel D was hardly changed in comparison with that of steel D tensile tested without hydrogen charging, although the tendency of the frequency of the KAM value of steel A was similar to that of steel D (Figure 14). These results suggested that the hydrogen embrittlement remarkably occurred owing to the acceleration of the localized deformation such as the vicinity of the packet and the lath boundaries in steel A, whereas steel D with hydrogen exhibited a similar fracture morphology as steel D without hydrogen because of the suppression of the localized deformation.

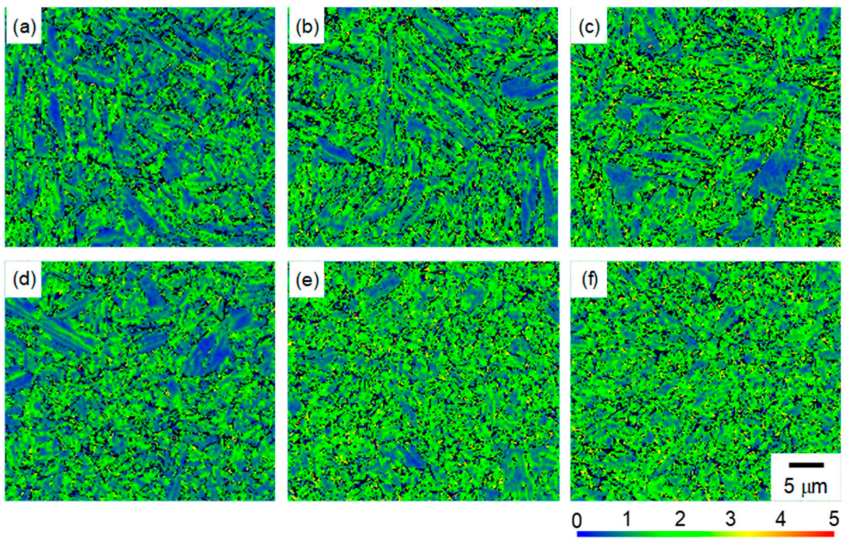

Figure 13. Kernel average misorientation (KAM) maps of (**a**,**d**) as heat treated, (**b**,**e**) deformed without hydrogen, and (**c**,**f**) deformed with hydrogen in steels (**a**–**c**) A and (**d**–**f**) D.

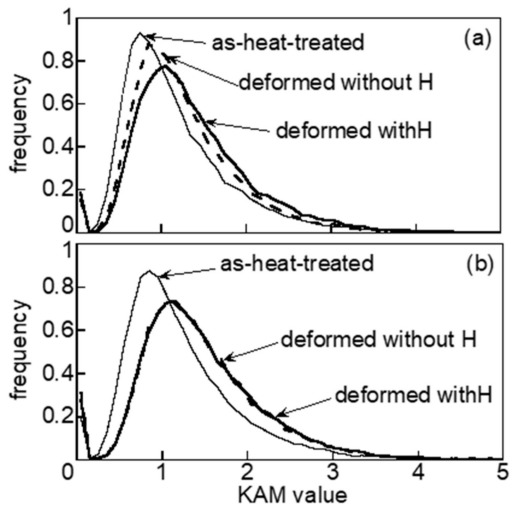

Figure 14. Variations in frequency as a function of kernel average misorientation (KAM) values of as-heat-treated, deformed without hydrogen, and deformed with hydrogen in steels (**a**) A and (**b**) D.

5. Conclusions

To apply the TRIP-aided martensitic steels for the automobile structural steels as third generation ultra high-strength steels, the effects of microalloying elements added for high hardenability on hydrogen embrittlement properties were investigated. The results are summarized as follows.

(1) Hydrogen embrittlement resistance was improved by the addition of alloying elements, especially 1.0 mass% chromium addition was most effective to improve the hydrogen embrittlement resistance.

(2) Higher hydrogen embrittlement resistance of the microalloyed TRIP-aided martensitic steels was obtained by (i) the suppression of initiation and propagation of voids and cracks at prior austenite grain, packet, block, and lath boundaries owing to the refinement of their sizes; (ii) the suppression of the hydrogen trapping at martensite matrix/cementite interfaces because of the hindered precipitation of cementite; and (iii) the restriction of martensitic transformation of retained austenite because of the high stability of retained austenite.

Author Contributions: Conceptualization, T.H., K.S., and A.N.; methodology, T.H.; formal analysis, T.H. and J.K.; investigation, T.H., J.K., and A.N.; resources, T.H. and E.A.; data curation, T.H.; writing—original draft preparation, T.H.; writing—review and editing, K.S. and E.A.; visualization, T.H.; project administration, T.H. All authors have read and agreed to the published version of the manuscript.

Funding: This work was conducted with financial support by the JKA, Suzuki Foundation, and Okayama Foundation for Science and Technology.

Conflicts of Interest: The authors declare no conflict of interest. The funders had no role in the design of the study; in the collection, analyses, or interpretation of data; in the writing of the manuscript; or in the decision to publish the results.

References

1. Zackay, V.F.; Parker, E.R.; Fahr, D.; Bush, R. The enhancement of ductility in high-strength steels. *Trans. Am. Soc. Met.* **1967**, *60*, 252–258.
2. Sugimoto, K.; Nakano, K.; Song, S.M.; Kashima, T. Retained austenite characteristics and stretch-flangeability of high-strength low-alloy TRIP type bainitic sheet steels. *ISIJ Int.* **2002**, *42*, 450–455. [CrossRef]
3. Hojo, T.; Kobayashi, J.; Sugimoto, K. Impact properties of low-alloy transformation-induced plasticity-steels with different matrix. *Mater. Sci. Technol.* **2016**, *32*, 1035–1042. [CrossRef]
4. Song, S.M.; Sugimoto, K.; Kandaka, S.; Futamura, A.; Kobayashi, M.; Masuda, S. Effects of prestraining on high-cycle fatigue strength of high-strength low alloy TRIP-aided steels. *Mater. Sci. Res. Int.* **2003**, *52*, 223–229. [CrossRef]

5. Hojo, T.; Sugimoto, K.; Mukai, Y.; Ikeda, S. Effects of aluminum on delayed fracture properties of ultra high strength low alloy TRIP-aided steels. *ISIJ Int.* **2008**, *48*, 824–829. [CrossRef]
6. Zhou, J.; Wang, B.; Huang, M.-d.; Cui, D. Effect of hot stamping parameters on the mechanical properties and microstructure of cold-rolled 22MnB5 steel strips. *Int. J. Miner. Metall. Mater.* **2014**, *21*, 544–555. [CrossRef]
7. Hagihara, Y. Evaluation of delayed fracture characteristics of high-strength bolt steels by CSRT. *ISIJ Int.* **2012**, *52*, 292–297. [CrossRef]
8. Takagi, S.; Hagihara, Y.; Hojo, T.; Urushihara, W.; Kawasaki, K. Comparison of hydrogen embrittlement resistance of high strength steel sheets evaluated by several methods. *ISIJ Int.* **2016**, *56*, 685–692. [CrossRef]
9. Chida, T.; Hagihara, Y.; Akiyama, E.; Iwanaga, K.; Takagi, S.; Hayakawa, M.; Ohishi, H.; Hirakami, D.; Tarui, T. Comparison of constant load, SSRT and CSRT methods for hydrogen embrittlement evaluation using round bar specimens of high strength steels. *ISIJ Int.* **2016**, *56*, 1268–1275. [CrossRef]
10. Tamura, I. *Steel Material Study on the Strength*; Nikkan-Kogyo Shinbun Ltd.: Tokyo, Japan, 1970.
11. Grossmann, M.A. Hardenability calculated from chemical composition. *Trans. AIME* **1942**, *150*, 227–255.
12. Kobayashi, J.; Ina, D.; Nakajima, Y.; Sugimoto, K. Effects of microalloying on the impact toughness of ultrahigh-strength TRIP-aided martensitic steels. *Metall. Mater. Trans. A* **2013**, *44*, 5006–5017. [CrossRef]
13. Dyson, D.J.; Holmes, B. Effect of alloying additions on the lattice parameter of austenite. *J. Iron Steel Inst.* **1970**, *208*, 469–474.
14. Valentini, R.; Tedesco, M.M.; Corsinovi, S.; Bacchi, L.; Villa, M. Investigation of mechanical tests for hydrogen embrittlement in automotive PHS steels. *Metals* **2019**, *9*, 934. [CrossRef]
15. Proctor, R.P.M.; Paxton, H.W. Effect of prior-austenite grain-size on stress-corrosion cracking susceptibility of AISI-4340 steel. *Asm Trans. Q.* **1969**, *62*, 989.
16. Nagao, A.; Hayashi, K.; Oi, K.; Mitao, S. Effect of uniform distribution of fine cementite on hydrogen embrittlement of low carbon martensitic steel plates. *ISIJ Int.* **2012**, *52*, 213–221. [CrossRef]
17. Cho, L.; Seo, E.J.; Sulistiyo, D.H.; Jo, K.R.; Kim, S.W.; Oh, J.K.; Cho, Y.R.; De Cooman, B.C. Influence of vanadium on the hydrogen embrittlement of aluminized ultra-high strength press hardening steel. *Mater. Sci. Eng. A* **2018**, *735*, 448–455. [CrossRef]
18. Takahashi, J.; Kawakami, K.; Kobayashi, Y.; Tarui, T. The first direct observation of hydrogen trapping sites in TiC precipitation-hardening steel through atom probe tomography. *Scr. Mater.* **2010**, *63*, 261–264. [CrossRef]
19. Sugimoto, K.; Murata, M.; Song, S.M. Formability of Al–Nb bearing ultra high-strength TRIP-aided sheet steels with bainitic ferrite and/or martensite matrix. *ISIJ Int.* **2010**, *50*, 162–168. [CrossRef]
20. Van Pham, D.; Kobayashi, J.; Sugimoto, K. Effects of microalloying on stretch-flangeability of ultrahigh-strength TRIP-aided martensitic steel sheets. *ISIJ Int.* **2014**, *54*, 1943–1951. [CrossRef]
21. Kobayashi, J.; Tonegawa, H.; Sugimoto, K. Cold formability of 22SiMnCrB TRIP-aided martensitic sheet steel. *Procedia Eng.* **2014**, *81*, 1336–1341. [CrossRef]
22. Hojo, T.; Koyama, M.; Terao, N.; Tsuzaki, K.; Akiyama, E. Transformation-assisted hydrogen desorption during deformation in steels: Examples of α′- and ε-martensite. *Int. J. Hydrog. Energy* **2019**, *44*, 30472–30477. [CrossRef]
23. Hojo, T.; Kobayashi, J.; Kochi, T.; Sugimoto, K. Effects of thermomechanical processing on microstructure and shear properties of 22SiMnCrMoB TRIP-aided martensitic steel. *Iron Steel Technol.* **2015**, *10*, 102–110.
24. Wang, M.; Akiyama, E.; Tsuzaki, K. Effect of hydrogen and stress concentration on the notch tensile strength of AISI 4135 steel. *Mater. Sci. Eng. A* **2005**, *398*, 37–46. [CrossRef]
25. Bhadeshia, H.K.D.H. Prevention of hydrogen embrittlement in steels. *ISIJ Int.* **2016**, *56*, 24–36. [CrossRef]
26. Momotani, Y.; Shibata, A.; Terada, D.; Tsuji, N. Effect of strain rate on hydrogen embrittlement in low-carbon martensitic steel. *Int. J. Hydrog. Energy* **2017**, *42*, 3371–3379. [CrossRef]
27. Chan, S.L.I.; Lee, H.L.; Yang, J.R. Effect of retained austenite on the hydrogen content and effective diffusivity of martensitic structure. *Metall. Trans. A* **1991**, *22*, 2579–2586. [CrossRef]
28. Gu, J.; Chang, K.D.; Fang, H.; Bai, B. Delayed fracture properties of 1 500 MPa bainite/martensite dual-phase high strength steel and its hydrogen traps. *ISIJ Int.* **2002**, *42*, 1560–1564. [CrossRef]